First report of vertically aligned (Sn,Ir)O$_2$:F solid solution nanotubes: Highly efficient and robust oxygen evolution electrocatalysts for proton exchange membrane based water electrolysis

Shrinath Dattatray Ghadge[a], Prasad P. Patel[a], Moni K. Datta[b,c], Oleg I. Velikokhatnyi[b,c], Pavithra M. Shanthi[a], Prashant N. Kumta[a,b,c,d,e,*]

[a] Chemical and Petroleum Engineering, Swanson School of Engineering, University of Pittsburgh, PA 15261, USA
[b] Department of Bioengineering, Swanson School of Engineering, University of Pittsburgh, PA 15261, USA
[c] Center for Complex Engineered Multifunctional Materials, University of Pittsburgh, PA 15261, USA
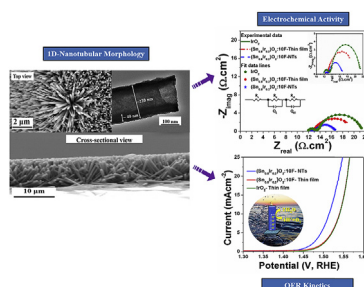[d] Mechanical Engineering and Materials Science, University of Pittsburgh, Pittsburgh, PA 15261, USA
[e] School of Dental Medicine, University of Pittsburgh, PA 15217, USA

HIGHLIGHTS

- 1D nanotube (NT) morphology explored for (Sn$_{0.8}$Ir$_{0.2}$)O$_2$:10F as OER electrocatalyst.
- Vertically aligned NTs first synthesized by a sacrificial template assisted approach.
- (Sn$_{0.8}$Ir$_{0.2}$)O$_2$:10F NTs show electrocatalytic activity superior to IrO$_2$ thin film.
- (Sn$_{0.8}$Ir$_{0.2}$)O$_2$:10F NTs exhibit low charge transfer resistance and higher ECSA.
- (Sn$_{0.8}$Ir$_{0.2}$)O$_2$:10F NTs display excellent stability in 1N H$_2$SO$_4$ PEM electrolyte.

GRAPHICAL ABSTRACT

ARTICLE INFO

ABSTRACT

One dimensional (1D) vertically aligned nanotubes (VANTs) of (Sn$_{0.8}$Ir$_{0.2}$)O$_2$:10F are synthesized for the first time by a sacrificial template assisted approach. The aim is to enhance the electrocatalytic activity of F doped (Sn,Ir)O$_2$ solid solution electrocatalyst for oxygen evolution reaction (OER) in proton exchange membrane (PEM) based water electrolysis by generating (Sn$_{0.8}$Ir$_{0.2}$)O$_2$:10F nanotubes (NTs). The 1D vertical channels and the high electrochemically active surface area (ECSA ~38.46 m^{2}g^{-1}) provide for facile electron transport. This results in low surface charge transfer resistance (4.2 Ω cm^2), low Tafel slope (58.8 mV dec^{-1}) and excellent electrochemical OER performance with ~2.3 and ~2.6 fold higher electrocatalytic activity than 2D thin films of (Sn$_{0.8}$Ir$_{0.2}$)O$_2$:10F and benchmark IrO$_2$ electrocatalysts, respectively. Furthermore, (Sn$_{0.8}$Ir$_{0.2}$)O$_2$:10F NTs exhibit excellent mass activity (21.67 A g^{-1}), specific activity (0.0056 mAcm^{-2}) and TOF (0.016 s^{-1}), which is ~2–2.6 fold higher than thin film electrocatalysts at an overpotential of 270 mV, with a total mass loading of 0.3 mg cm^{-2}. In addition, (Sn$_{0.8}$Ir$_{0.2}$)O$_2$:10F NTs demonstrate remarkable electrochemical durability - comparable to thin films of (Sn$_{0.8}$Ir$_{0.2}$)O$_2$:10F and pure IrO$_2$, operated under identical testing conditions in PEM

water electrolysis. These results therefore indicate promise of $(Sn_{0.8}Ir_{0.2})O_2$:10F NTs as OER electrocatalysts for efficient and sustainable hydrogen production.

1. Introduction

The identification, synthesis and development of high performance oxygen evolution reaction (OER) electrocatalysts for proton exchange membrane (PEM) based water electrolysis with reduced noble-metal (e.g. IrO_2, RuO_2 and Pt/C) content or with non-noble metal electrocatalysts is a major challenge facing the PEM fuel cell area. Added to this is the challenge of the system exhibiting excellent electrocatalytic activity and faster reaction kinetics along with the prolonged stability during electrolysis operation together representing the foremost challenge facing researchers in the OER electrocatalyst research area [1–4]. In an attempt to make major strides, we have exploited the theoretical first principles electronic structure calculations and have identified several highly active OER electrocatalysts with substantial reduction in the noble metal content of IrO_2/RuO_2 (i.e. ~ 70–80 mol. %) [1,4–6]. Accordingly, the solid solution of electrochemically non-active parent oxides with significantly lower noble metal (up to ~ 80 mol % Ir) content such as fluorine (F) doped binary and ternary solid solution oxides, synthesized in 2D thin films architectures have displayed comparable electrocatalytic activity and stability to that of pure IrO_2 [1,5]. The thin film approach for electrocatalyst synthesis is well known and beneficial due to several reasons. In contrast to powder based electrocatalysts, the film composition can be precisely controlled by the metal ions added to the precursor solutions, which is not easily accessible by conventional high temperature based pathways [7]. In addition, the thin film electrocatalysts architecture extensively lack the porous structure which results in facile mass transport of the evolving gases [7]. Also, as thin film electrocatalysts are directly fabricated/grown on the substrate or current collector, it eliminates requirement of any conductive additives or expensive binders, which are predominantly required in the powder based electrocatalysts [8,9].

Based on the work conducted to date, for further enhancing the electrocatalytic activity of these reduced noble metal containing 2D thin film solid solution electrocatalysts, we have embarked on the challenge to tailor the material length scales into one-dimensional (1D) nanoscale motifs. Accordingly, 1D vertically aligned nanotubular (VANT) architectures of electrochemically active systems have been generated in an attempt to improve the reaction kinetics and correspondingly, the nanotubular structures exhibit superior electrocatalytic activity towards the water splitting reaction [2,10–12].

In recent years, 1D nanostructures with nanotube (NT) as well as nanowire (NW) based morphologies have been widely studied for the application of electrocatalysts such as Pt NTs [8], nitrogen-containing carbon nanotubes (NCNTs) [13], Pt-Ru/Co NWs [14], Co_4N NWs [9], Pt–Ni–TiO_2 NTs [15] etc. in the water splitting and direct methanol fuel cell (DMFC) research area. Assembling the nanoparticles of electrocatalyst into tubular nanostructures offers various added benefits such as high active surface area, high aspect ratios (length-to-width ratio), dense catalytic sites - which expedite the catalytic activity for surface electrochemical reactions [2,8,16]. For example, Pt nanostructures with 1D nanotubular architectures have demonstrated ~ 1.4 times higher electrochemical active surface area than Pt black; leading to significantly improved catalytic activity (4.4 fold) towards oxygen reduction reaction [8,17]. In addition, 1D vertically oriented nanostructures offer sufficient porosity between the adjacent 1D nanostructures which facilitates mass as well as charge transport including superior electrocatalyst-electrolyte contact due to the easy accessibility of electrolyte molecules into the deep portion of the electrode/catalyst surface, which ultimately bolsters the electrocatalytic performance [2,11,16,18,19]. Besides, due to the presence of vertical channels, the 1D vertically aligned motifs expedite the facile charge transport pathway between the catalyst surface and the current collector by directing effective channels in the catalyst electrodes which decreases the surface charge transfer resistance (R_{ct}) and thus, enhancing the electronic conductivity i.e. reaction kinetics on the electrocatalyst surface [8,9]. Moreover, the1D nanostructures also offer the unique prospect of developing the electrocatalyst nanostructures directly grown on the current collectors - without any requirement of conductive additives or binders [8,9].

It has been reported that the electrocatalysts with similar composition yet different morphologies significantly influence the electrocatalytic activity due to alteration of the charge transport properties, electrochemically active surface area and diffusion of reactants and products during the reaction process [20,21]. Therefore, in the present study, we have explored the 'nanotube (NT) structured-1D morphology for the solid solution $(Sn_{1-x}Ir_x)O_2$:10F (x = 0.2) electrocatalyst'; comprising earth abundant tin oxide (SnO_2), fluorine (F) and ultra-low noble metal (Iridium, Ir) content, for the very first time to the best of our knowledge. Accordingly, we have studied and compared the electrochemical performance for OER of the solid solution metal oxide based electrocatalysts of different architectures (nanostructured 2D thin film and 1D nanotubes) and correlated their materials length scale parameters to the electrocatalytic properties. We have already studied the system as an optimum 2D thin film composition [$(Sn_{0.8}Ir_{0.2})O_2$:10F] for OER in PEM based water electrolysis in our previously published report [1]. Thus, herein, a versatile sacrificial template-assisted approach has been employed to fabricate $(Sn_{0.8}Ir_{0.2})O_2$:10F VANTs on titanium (Ti) substrate. In order to generate 1D nanomaterials, various methods such as physical vapor deposition [22], thermal decomposition [23], and vapor-liquid-solid deposition [24,25] etc. have been reported. Among these techniques, the template-assisted or template-directed approach is simplistic, cost-effective and well known for the reliable fabrication of uniformly arranged one-dimension architectures, offering efficient control over size and shape of the various nano-structured materials [26–28]. Accordingly, in the present study, 1D $(Sn_{0.8}Ir_{0.2})O_2$:10F VANTs are synthesized via ZnO nanowires as a sacrificial template-assisted approach. The as-synthesized 1D $(Sn_{0.8}Ir_{0.2})O_2$:10F VANTs exhibit superior electrocatalytic activity toward OER with lower surface charge transfer resistance (R_{ct}), lower Tafel slope, higher electrochemical active surface area (ECSA), higher specific activity and turnover frequency (TOF) than the corresponding 2D thin film architectures of $(Sn_{0.8}Ir_{0.2})O_2$:10F and state-of-the art IrO_2 electrocatalysts. This research outlines the synthesis of vertically aligned nanotubes, structural and detailed electrochemical characterization of the $(Sn_{0.8}Ir_{0.2})O_2$:10F nanotubular electrocatalyst.

2. Experimental methodology

2.1. Synthesis of electrocatalysts

2.1.1. Vertically aligned nanotubes (VANTs) of $(Sn_{1-x}Ir_x)O_2$:10 wt% F (x = 0.2)

2.1.1.1. Synthesis of ZnO based nanowires (NWs) as sacrificial template. Synthesis of $(Sn_{1-x}Ir_x)O_2$:10F VANTs has been achieved using ZnO NWs as a sacrificial template. ZnO NWs were grown on titanium (Ti) foil (substrate) by the hydrothermal method [2,18,29–31]. Prior to growing the NWs, the Ti foil (0.5 cm × 2 cm, Aldrich) was thoroughly cleaned by ultra-sonication in a mixture of acetone, ethanol and deionized water (18 MΩ cm, MilliQ Academic, Millipore). 5.5 mM of zinc acetate solution in ethanol (anhydrous, 200

proof, 99.5 + %, Aldrich) was then spin-coated on the cleaned Ti substrate using Specialty coating Systems Inc., Model P6712 at 500 rpm for 40 s and then heated (for drying) at 125 °C. The Ti foil containing the zinc acetate layer was then subjected to heat treatment in air at 340 °C for 20 min, which resulted in the seed layer of ZnO on Ti foil. In order to grow the ZnO NW template from the ZnO seed layer, the Ti foil containing ZnO seed layer was placed in a sealed container - enclosing the growth solution of zinc nitrate hexahydrate (0.05 M, Alfa Aesar), hexamethylenetetramine (HMTA, 0.025 M, Alfa Aesar), polyethylenimine (5.0 mM, end-capped, molecular weight 800 gmol^{-1} LS, Aldrich) and ammonium hydroxide (0.35 M). Next, this sealed container was placed in a water bath, preheated to 90 °C for 6 h. The formed nanowires were then carefully washed with ethanol and D.I. water followed by drying at 50 °C for 6 h.

2.1.1.2. Synthesis of SnO_2 VANTs. Vertically aligned SnO_2 nanotubes on Ti substrate were synthesized by placing the ZnO NWs grown Ti substrate in an aqueous solution consisting of 3 ml of 0.15 M ammonium hexafluorostannate(AHFS) [$(NH_4)_2SnF_6$, Aldrich], 1 mL of 0.5 M boric acid (H_3BO_3, Aldrich) and 1 mL of D.I. water at 26 °C for 30 min. In this process, the ZnO NWs template (formed on Ti substrate) was replaced by SnO_2 nanotubes; retaining the pre-formed vertically aligned morphology of ZnO which has been further confirmed by the experimental techniques discussed in the results section. After 30 min, the resultant SnO_2 VANTs were washed with D.I. water followed by drying at 50 °C for 6 h.

2.1.1.3. Synthesis of $(Sn_{1-x}Ir_x)O_2$:10F VANTs (x = 0.2). The IrO_2 and F containing SnO_2 solid solution [$(Sn_{1-x}Ir_x)O_2$:10F] was generated by infiltrating Ir and F containing precursors into the SnO_2 VANTs. For infiltration of Ir and F into SnO_2 VANTs, the Ti substrate on which SnO_2 VANTs were formed, was placed in a solution of iridium tetrachloride ($IrCl_4$, 99.5%, Alfa Aesar) and ammonium fluoride (NH_4F, 98%, Alfa Aesar), prepared in DI water corresponding to the desired composition [i.e. $(Sn_{0.8}Ir_{0.2})O_2$:10 wt% F]. The Ti substrate containing SnO_2 NTs infiltrated with $IrCl_4$ and NH_4F solution was then subjected to heat treatment at 400 °C for 4h to form $(Sn_{1-x}Ir_x)O_2$:10F VANTs on Ti foil. Schematic illustration of the synthesis process for generating $(Sn_{1-x}Ir_x)O_2$:10F NTs (x = 0.2) with electrocatalyst loading of ~0.3 mg cm^{-2} on Ti substrate is depicted in Fig. 1.

2.1.2. Thin films of $(Sn_{1-x}Ir_x)O_2$:10 wt% F (x = 0.2) and IrO_2

The electrochemical performance of the synthesized 1D $(Sn_{0.8}Ir_{0.2})O_2$:10F VANTs were compared to 2D thin film architectures. Hence, thin films of $(Sn_{0.8}Ir_{0.2})O_2$:10F and pure IrO_2 were synthesized on Ti foil following the protocol described in detail in an earlier study reported by us [1]. In brief, Iridium tetrachloride ($IrCl_4$, 99.5%, Alfa Aesar), tin (II) chloride dihydrate [$SnCl_2.2H_2O$, 98%, Alfa Aesar] and ammonium fluoride (NH_4F, 98%, Alfa Aesar) were used as the sources for Ir, Sn and F, respectively. $IrCl_4$ and $SnCl_2.2H_2O$ stock solutions with the desired composition are prepared in absolute ethanol. NH_4F stock solution was made by dissolving NH_4F in ethanol–DI water mixture with a volume ratio of 5: 1. The above stock solutions are then mixed together according to the desired composition of the electro-catalyst material [$(Sn_{1-x}Ir_x)O_2$:10 wt% F, x = 0.2] and then spin coated (Speciality coating Systems Inc. Model P6712) onto pretreated (sandblasted and then etched in boiling HCl for 30 min) substrate-titanium foil (Alfa Aesar) having area of ~1 cm^2 (0.5 cm × 2 cm). Spin coating was performed with a rotating speed of 500 rpm for 10 s. Suitable amount of the precursors was selected to achieve a desired electrocatalyst loading of ~0.3 mg cm^{-2}. The precursors deposited Ti substrate was then dried in air at 60 °C for 2 h. The dried substrate was then subjected to thermal treatment in air at 400 °C for 4 h, which resulted in the formation of $(Sn_{0.8}Ir_{0.2})O_2$:10F thin film on the Ti foil. Similar approach was employed to synthesize pure IrO_2 thin film on Ti substrates.

2.2. Electrocatalyst materials characterization

2.2.1. Structural characterization

The crystalline structure of the resulting materials were characterized using x-ray diffraction (XRD) analysis which has been performed to both qualitatively and quantitatively analyze the as-prepared electrocatalysts. XRD is performed using the Philips XPERT PRO system employing CuK$_\alpha$ radiation source (λ = 0.15406 nm) at an operating current and voltage of 40 mA and 45 kV, respectively. The least square refinement techniques have been utilized to determine the molar volume of the electrocatalyst.

The microstructure of $(Sn_{0.8}Ir_{0.2})O_2$:10F NTs has been studied by performing scanning electron microscopy (SEM). Energy dispersive x-ray spectroscopy (EDX) analyzer (attached with the SEM machine) has been used for conducting quantitative elemental analysis. Philips XL-30FEG equipped with an EDX detector system comprising of an
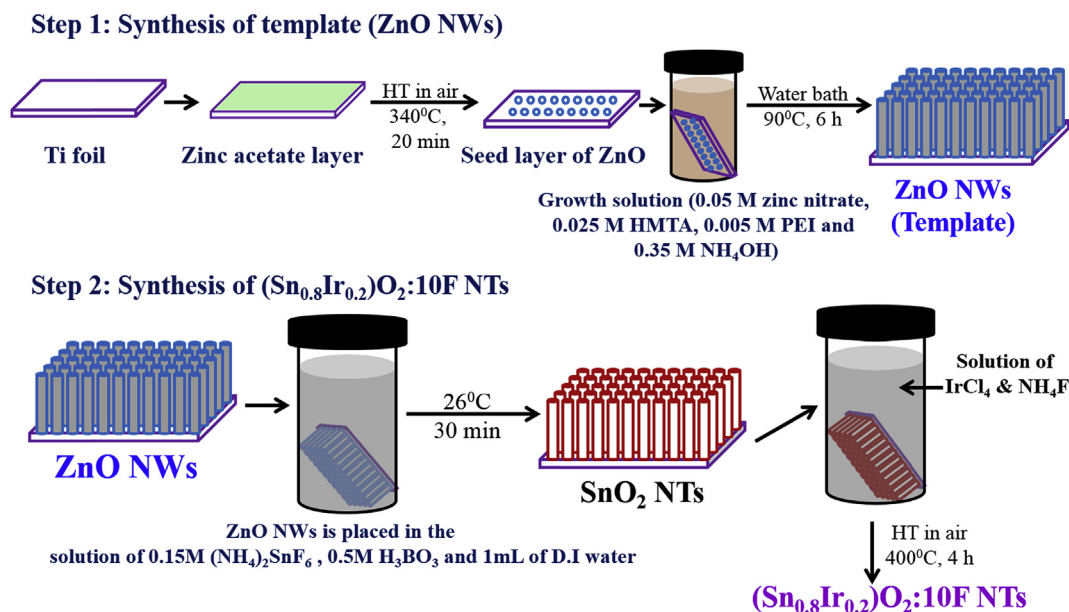

Step 1: Synthesis of template (ZnO NWs)

Ti foil → Zinc acetate layer → HT in air 340°C, 20 min → Seed layer of ZnO → Growth solution (0.05 M zinc nitrate, 0.025 M HMTA, 0.005 M PEI and 0.35 M NH$_4$OH) — Water bath 90°C, 6 h → ZnO NWs (Template)

Step 2: Synthesis of $(Sn_{0.8}Ir_{0.2})O_2$:10F NTs

ZnO NWs → ZnO NWs is placed in the solution of 0.15M $(NH_4)_2SnF_6$, 0.5M H_3BO_3 and 1mL of D.I water — 26°C 30 min → SnO_2 NTs → Solution of $IrCl_4$ & NH_4F — HT in air 400°C, 4 h → $(Sn_{0.8}Ir_{0.2})O_2$:10F NTs

Fig. 1. Schematic illustration of the synthesis process of $(Sn_{0.8}Ir_{0.2})O_2$:10F NTs using the template assisted approach.

ultrathin beryllium window and Si(Li) detector, operating at 20 kV was used for the corresponding evaluation of the microstructure as well as conducting elemental and x-ray mapping analysis of the electrocatalyst. Transmission electron microscopy (TEM) (JEOL JEM-2100F system operating at 200 kV) was performed to analyze the structure of the as-prepared nanotubes. Energy Dispersive Spectroscopy (EDS) as well as line scan analysis was conducted for the elemental analysis and investigation of the solid solution formation of as-prepared $(Sn_{0.8}Ir_{0.2})O_2$:10F NTs. The quantitative elemental analysis was also carried out by utilizing inductively coupled plasma optical emission spectroscopy (ICP-OES, iCAP 6500 duo Thermo Fisher).

To investigate the oxidation states of Sn and Ir in the as-synthesized electrocatalysts, X-ray photoelectron spectroscopy (XPS) was performed. ESCALAB 250 Xi system (Thermo Scientific) equipped with a monochromatic Al Kα X-ray source was utilized to perform XPS analysis. The standard analysis spot of $400 \times 400\,\mu m^2$ was defined by the micro-focused X-ray source. The mentioned XPS system is operated at room temperature in an ultra-high vacuum chamber with the base pressure less than 5×10^{-10} mbar. Calibration of the binding energy (BE) scale was done to generate < 50 meV deviations of the three standard peaks from their standard values. The aliphatic C1s peak was observed at 284.6 eV. High-resolution elemental XPS data in C2p, S2p, Mg2p, and Zn2p regions were acquired with the analyzer pass energy set to 20 eV (corresponding to energy resolution of 0.36 eV) and the step size was set to 0.1 eV. Fitting of the elemental spectra based on the calibrated analyzer transmission functions, Scofield sensitivity factors and effective attenuation lengths for photoelectrons from the standard TPP-2M formalism was conducted using the Avantage software package (Thermo Fisher Scientific).

2.2.2. Electrochemical characterization

Electrochemical characterization of the as-prepared electrocatalysts (total electrocatalyst loading ~ 0.3 mg cm^{-2}) was carried out in a three electrode configuration at 40 °C (maintained using a Fisher Scientific 910 Isotemp refrigerator circulator) on a VersaSTAT 3 (Princeton Applied Research) electrochemical workstation. 1 N sulfuric acid (H_2SO_4) was used as the electrolyte solution and also as a proton source for oxygen evolution reaction (OER). Oxygen gas from the electrolyte solution was expelled by purging the electrolyte solution with ultrahigh pure (UHP) argon gas (Matheson) for ~ 15 min [32]. The as-prepared electrocatalysts were used as a working electrode (anode), Pt wire (Alfa Aesar, 0.25 mm thick, 99.95%) was used as the counter electrode (cathode) and mercury/mercurous sulfate (Hg/Hg_2SO_4) electrode (XR-200, Hach) having a potential of $+0.65$ V with respect to reversible hydrogen electrode (RHE) was used as the reference electrode. All the potential values reported in the present study are determined with respect to RHE and calculated from the formula [4,33,34]: $E_{RHE} = E_{Hg/Hg2SO4} + E^0_{Hg/Hg2SO4} + 0.059$ pH, where E_{RHE} is the potential versus RHE. $E_{Hg/Hg2SO4}$ is the potential measured against the Hg/Hg_2SO_4 reference electrode and $E^o_{Hg/Hg2SO4}$ is the standard electrode potential of Hg/Hg_2SO_4 reference electrode ($+0.65$ V vs RHE).

2.2.2.1. Electrochemical impedance spectroscopy (EIS).

To determine the solution resistance (R_s), electrode resistance (R_e), ohmic resistance (R_Ω) ($R_\Omega = R_s + R_e$) and the surface charge transfer resistance (R_{ct}) of the as-prepared electrocatalysts, EIS has been performed. The polarization curves of the synthesized electrocatalysts have been iR_Ω ($iR_\Omega = iR_s + iR_e$) corrected utilizing the ohmic resistance (R_Ω) obtained from EIS analysis. The EIS was performed in the frequency range of 100 mHz-100 kHz (Amplitude = 10 mV) using the electrochemical work station (Versa STAT 3, Princeton Applied Research) in 1 N H_2SO_4 electrolyte solution at 40 °C, at ~ 1.5 V (vs RHE). The ZView software from Scribner Associates employing the $R_s(R_eQ_1)(R_{ct}Q_{dl})$ equivalent circuit was used to model the impedance data for OER. In this model R_s is in series with the parallel combination

of the R_e and Q_1 and further in series with the parallel combination of the R_{ct} and Q_{dl}. The components of this model are [1,34].

R_s = Resistance faced at high frequency due to surface charge transfer in electrolyte solution,

R_e = Resistance for electron transfer from the electrode to current collector (Ti foil),

R_{ct} = Surface charge transfer resistance (i.e., polarization resistance) for electrocatalyst-electrolyte interface,

Q_1 = Constant phase element, and

Q_{dl} = Contribution from both the double layer capacitance and pseudo capacitance.

2.2.2.2. Linear scan polarization.

The electrochemical performance of the as-prepared electrocatalysts (for OER) was studied by conducting linear scan polarization in 1 N H_2SO_4 electrolyte solution with a scan rate of 10 mV^{-1} at 40 °C. Polarization curves of electrocatalysts were iR_Ω corrected, as described above in the EIS section. The current density at ~ 1.5 V (vs RHE, which is the typical potential used for measuring the electrochemical activity of the electrocatalyst for OER [35]) in iR_Ω corrected polarization curves was used for comparing the electrochemical performance of the different electrocatalysts. In order to study and compare the reaction kinetics of the as-synthesized electrocatalysts, Tafel plots are developed after iR_Ω correction using the equation $\eta = a + b \log i$ [i.e. plot of overpotential (η) vs log current (log i)] [4,36]. In this equation, 'a' and 'b' represent the exchange current density and Tafel slope, respectively. Further, cyclic voltammetry (CV) curves were recorded to assess the electrochemically active surface area (ECSA) of the as-prepared electrocatalysts with various scan rates in the potential range from 0.1 to 1.2 V (vs RHE). The differences in current density ($j_{anode} - j_{cathode}$) at 0.7 V (vs RHE) are plotted against the scan rate (mV s^{-1}) and fitted to a linear regression [37,38] to obtain the corresponding C_{dl} and ECSA values. In addition, the intrinsic OER activity of the as-prepared electrodes was investigated by calculating specific activity, mass activity, turnover frequency (TOF) and normalization of current densities by ECSA (m^{2}g^{-1}) and electrocatalyst mass loading (see the Supplementary Information for calculation details.)

2.2.2.3. Electrochemical stability test.

Chronoamperometry (CA) test (current vs time) was performed to study the electrochemical stability of as-synthesized electrocatalysts for the long term operation. In the CA test, the working electrode was maintained for 24 h in 100 ml electrolyte solution of 1 N H_2SO_4 at 40 °C under a constant voltage of ~ 1.5 V (vs RHE). In order to determine the amount of Ir and Sn leached out from the working electrode, electrolyte solutions (10 ml) collected after 24 h of CA test were subjected to elemental analysis in an inductively coupled plasma optical emission spectroscopy (ICP-OES, iCAP 6500 duo Thermo Fisher). This analysis is beneficial to understand the robustness and corrosion resistance of the as-prepared electrocatalysts towards long term OER in PEM water electrolysis. In addition, the post stability characterizations (XRD and XPS) were carried out to investigate the structural robustness of $(Sn_{0.8}Ir_{0.2})O_2$:10F NTs during OER.

3. Results and discussion

3.1. Experimental characterization of electrocatalysts

3.1.1. Structural characterization of electrocatalysts

3.1.1.1. X-ray diffraction (XRD) analysis. The XRD pattern of SnO_2 NTs (Fig. 2) shows the rutile type tetragonal structure and the patterns match with the reported patterns confirming the formation of SnO_2 [1,39]. Similarly, the XRD pattern of $(Sn_{0.8}Ir_{0.2})O_2$:10F NTs reveals the rutile type tetragonal structure similar to that of pure SnO_2 NTs, which
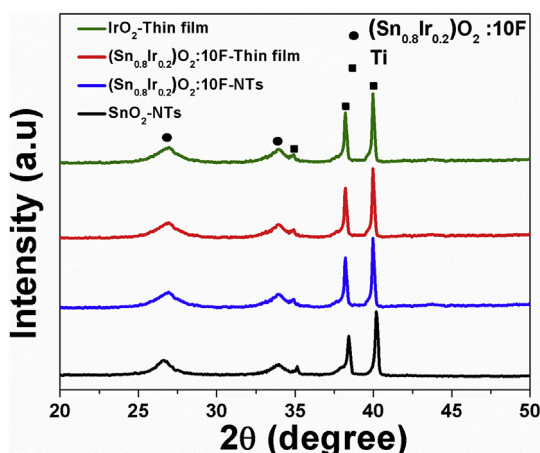
Fig. 2. The XRD patterns of nanostructured 2D thin films of pure IrO_2 and $(Sn_{0.8}Ir_{0.2})O_2$:10F; and nanotubes (NTs) of pure SnO_2 and $(Sn_{0.8}Ir_{0.2})O_2$:10F electrocatalysts fabricated on Ti foil.

suggests the formation of a single phase homogeneous solid solution of SnO_2 and IrO_2 [i.e. $(Sn,Ir)O_2$:F] without any other peaks of Sn or Ir based compounds or any undesired phase separation [1,39]. The XRD patterns of 2D thin films of pure IrO_2 and $(Sn_{0.8}Ir_{0.2})O_2$:10F generated

on Ti foil (Fig. 2) also show similar XRD patterns as reported earlier, suggesting the successful formation of fully crystalline IrO_2 and solid solution of SnO_2 and IrO_2 [i.e. $(Sn,Ir)O_2$:F], respectively [1]. Furthermore, the molar volume of $(Sn_{0.8}Ir_{0.2})O_2$:10F NTs, calculated using the least square refinement technique is ~ 21.18 $cm^3 mol^{-1}$ which is comparable to that of 2D thin film of $(Sn_{0.8}Ir_{0.2})O_2$:10F as reported in the previous study [1]. In the various OER electrocatalysts studies it has been observed and reported that the electro-catalytic activity of IrO_2 starts decreasing from annealing temperatures of 400 °C–600 °C while more stable electrodes were formed at T ≥ 400 °C [40–42]. Furthermore, according to the study conducted by Geiger et al. [41] it has been concluded that the electrodes synthesized at 400 °C-500 °C are identified as the most promising for acidic OER on the basic of their intrinsic activity and catalytic dissolution rate. Therefore, in the present study, based on these studies as well as previous acidic OER studies by our group [1,6,39,43], we have selected the optimum annealing temperature of 400 °C to synthesize the fully crystalline electrocatalysts, possessing excellent catalytic activity as well as stability for acidic OER.

3.1.1.2. SEM and TEM analysis. The morphology of SnO_2 NTs (Fig. 3A) and $(Sn_{0.8}Ir_{0.2})O_2$:10F NTs (Fig. 3B) has been studied by performing the SEM analysis. Accordingly, the SEM image of SnO_2 NTs (Fig. 3A) shows the highly dense, well-spaced and vertically aligned nanotubes, suggesting the formation of nanotubular morphology. Similarly, the
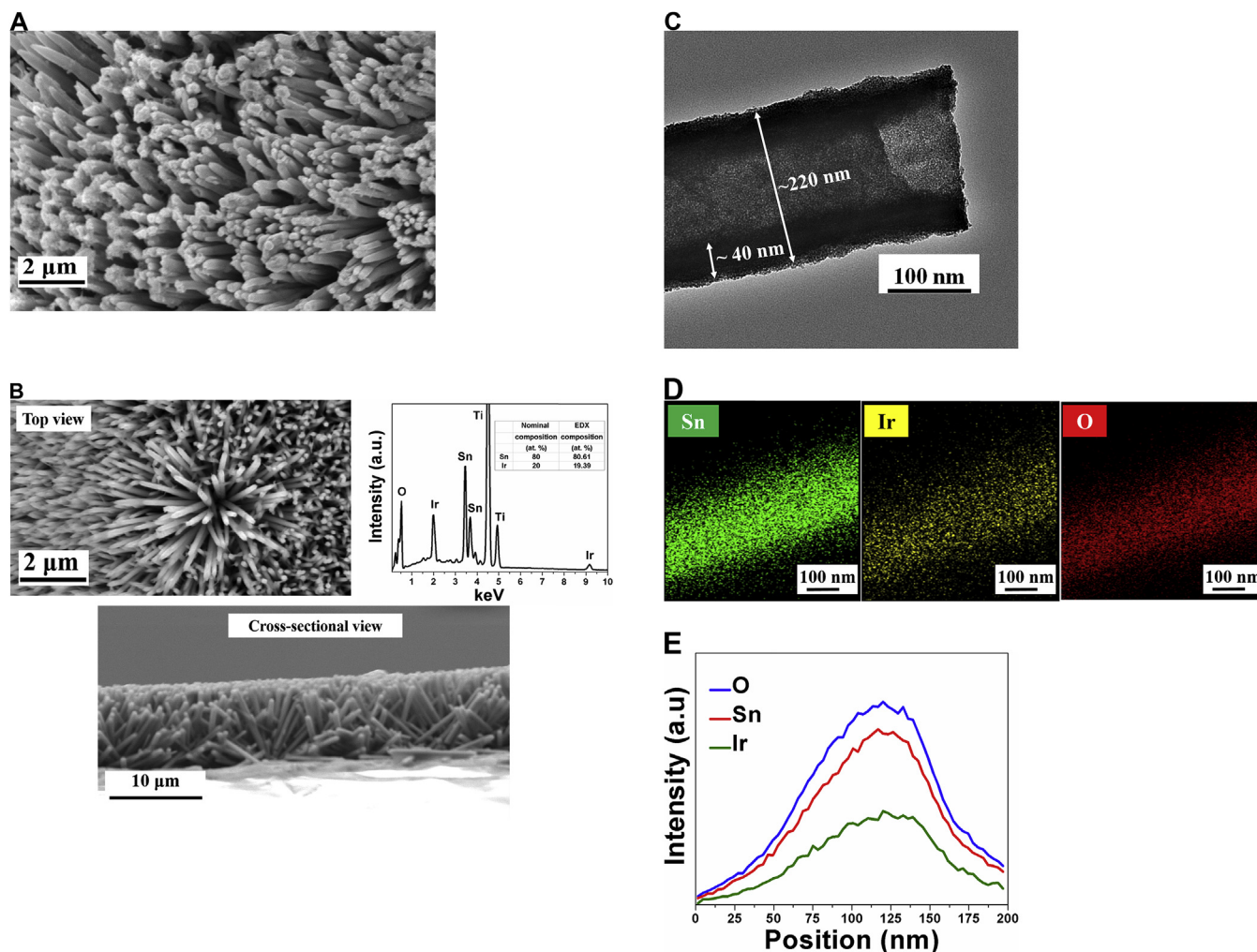

Fig. 3. (A) The SEM micrograph showing top view of SnO_2 NTs, (B) The SEM micrograph showing top view, cross-sectional view and EDX spectrum of $(Sn_{0.8}Ir_{0.2})O_2$:10F NTs, (C) The bright field TEM image of $(Sn_{0.8}Ir_{0.2})O_2$:10F NT, (D) EDS elemental mapping of Sn, Ir and O of the $(Sn_{0.8}Ir_{0.2})O_2$:10F NT, and (E) line scan analysis across a $(Sn_{0.8}Ir_{0.2})O_2$:10F NT.

top and cross-sectional views of $(Sn_{0.8}Ir_{0.2})O_2$:10F NTs (Fig. 3B) also show highly dense, well-spaced and vertically aligned nanotubes (VANTs), suggesting the retention of the nanotubular morphology of SnO_2 upon the solid solution formation of F incorporated SnO_2 and IrO_2 [(Sn,Ir)O_2:F], (similar to that of pure SnO_2 as shown in Fig. 3A). The SEM image of $(Sn_{0.8}Ir_{0.2})O_2$:10F NTs clearly shows the formation of vertically aligned nanotubes having diameter and length of ~220 nm and ~10 μm, respectively, without the presence of any other morphologies. Herein, based on the SEM images and the geometrical data, approximate specific surface area (SSA) of $(Sn_{0.8}Ir_{0.2})O_2$:10F nanotubes has been calculated (see the Supplementary Information for calculation details). The approximate SSA of $(Sn_{0.8}Ir_{0.2})O_2$:10F NTs was obtained as 7.33 m^2g^{-1}.

The presence of Sn and Ir in $(Sn_{0.8}Ir_{0.2})O_2$:10F NTs has been further verified by conducting EDX analysis (Fig. 3B). Correspondingly, EDX analysis showed that the measured elemental composition of Sn (80.61%) and Ir (19.39%) was very close to the chosen nominal composition of Sn (~80 at. %) and Ir (~20 at. %). In addition, inductively coupled plasma optical emission spectroscopy (ICP-OES) analysis showed the atomic % of Sn and Ir as 81.55 and 18.45 respectively. These atomic % obtained from the ICP-OES are almost consistent with the values obtained from the EDX (Fig. 3B). Thus, the ICP and EDX analysis provided strong corroboration of the nominal composition [i.e. Sn (80 at.%) and Ir (20 at.%)]. Furthermore, the TEM image obtained on a representative $(Sn_{0.8}Ir_{0.2})O_2$:10F NT (Fig. 3C) shows the nanotubular geometry of $(Sn_{0.8}Ir_{0.2})O_2$:10F with a diameter of ~220 nm and a wall thickness of ~40 nm, respectively. Fig. 3D shows the EDS elemental mapping images of Sn, Ir and O for a $(Sn_{0.8}Ir_{0.2})O_2$:10F NT, suggesting that the Sn and Ir elements are well and uniformly distributed in the as-synthesized NT. There is also no segregation of any elements at any specific region. In addition, it is quite clear from the line scan analysis (Fig. 3E) that there is a homogenous dispersion of Sn and Ir in the as-synthesized $(Sn_{0.8}Ir_{0.2})O_2$:10F NT. This EDS and line scan analysis further reveals the formation of a single phase homogeneous solid solution of SnO_2 and IrO_2 [i.e. (Sn,Ir)O_2:F], denying the possibility of IrO_2 coverage on the SnO_2 bulk phase.

3.1.1.3. X-ray photoelectron spectroscopy (XPS) analysis.

XPS analysis has been conducted to identify the valence states of Ir and Sn in $(Sn_{0.8}Ir_{0.2})O_2$:10F NTs, SnO_2 NTs, and thin films of $(Sn_{0.8}Ir_{0.2})O_2$:10F and IrO_2. As shown in Fig. 4A, the XPS spectrum of Ir of $(Sn_{0.8}Ir_{0.2})O_2$:10F NTs and thin films of $(Sn_{0.8}Ir_{0.2})O_2$:10F and IrO_2 show the presence of Ir $4f_{5/2}$ and Ir $4f_{7/2}$ doublet. The XPS spectra of Ir of IrO_2 shows the presence of Ir $4f_{5/2}$ and Ir $4f_{7/2}$ doublet with binding energy values of ~64.58 eV and ~61.68 eV, respectively [4]. As compared to pure IrO_2, in the case of $(Sn_{0.8}Ir_{0.2})O_2$:10F thin film and NTs, the positive shift of ~0.7–0.9 eV towards higher binding energy in the Ir $4f_{5/2}$ and Ir $4f_{7/2}$ doublet positions was observed, which is consistent with the previously reported results for F doped solid solution electrocatalysts [1,4,35]. This positive shift suggests the likely binding of the fluorine in the $(Sn_{0.8}Ir_{0.2})O_2$:10F NTs and thin film electrocatalyst, which contributes to the modification of the electronic structure of $(Sn_{0.8}Ir_{0.2})O_2$:10F as a result of the solid solution formation and incorporation of F [1,4]. Fig. 4B shows the XPS spectra of Sn of SnO_2 NTs, $(Sn_{0.8}Ir_{0.2})O_2$:10F NTs and $(Sn_{0.8}Ir_{0.2})O_2$:10F thin film. Pure SnO_2 exhibits the binding energy values of ~495.37 eV and ~486.95 eV for Sn $3d_{3/2}$ and Sn $3d_{5/2}$, respectively [44,45], whereas $(Sn_{0.8}Ir_{0.2})O_2$:10F film and NTs demonstrate the positive shift of ~0.7 eV towards higher binding energy values, similar to as reported in earlier studies [1,35]. The presence of F in the as-synthesized $(Sn_{0.8}Ir_{0.2})O_2$:10F NTs and film could not be unequivocally determined by XPS, EDX (Fig. 3C) and elemental mappings (Fig. 3D) which is consistent with the earlier publications on Sn/Mn/Nb substituted IrO_2 electrocatalysts [1,4,5,35]. However, the observed positive shifts in the binding energy values w.r.t. pure SnO_2 and IrO_2 can indeed be an indicator of the of F incorporation into the lattice of

solid solution oxide. This implies the modification of the electronic structure due to the formation of solid solution electrocatalyst as well as due to the existence of fluorine in the solid solution lattice which results in the superior binding attributed to the higher electronegativity of fluorine [1,4,46].

3.1.2. Electrochemical characterization of electrocatalysts

Fig. 5A shows the electrochemical impedance spectroscopy (EIS) of $(Sn_{0.8}Ir_{0.2})O_2$:10F NTs along with the synthesized 2D thin films of identical composition of $(Sn_{0.8}Ir_{0.2})O_2$:10F and pure IrO_2 electrocatalysts used as the benchmark electrocatalyst measured at ~1.5V (*vs* RHE) in the electrolyte solution of 1 N H_2SO_4 at 40 °C (inset: EIS equivalent circuit and magnified views of EIS). As discussed in the experimental section, the $R_s(R_eQ_1)(R_{ct}Q_{dl})$ equivalent circuit model in which R_s is in series with the parallel combination of the R_e and Q_1 and further in series with the parallel combination of the R_{ct} and Q_{dl} was utilized to determine the R_e, R_s and R_{ct}, which are correspondingly tabulated in Table 1. As shown in Fig. 5A the surface charge transfer resistance (R_{ct}), determined from the diameter of the semi-circle in the low frequency region of the EIS plot of $(Sn_{0.8}Ir_{0.2})O_2$:10F NTs (R_{ct} ~4.2 Ω cm^2) is significantly lower than $(Sn_{0.8}Ir_{0.2})O_2$:10F thin film (R_{ct} ~6.7 Ω cm^2) as well as the thin film of pure IrO_2 (R_{ct} ~8 Ω cm^2), suggesting the lower activation polarization and higher electronic conductivity of $(Sn_{0.8}Ir_{0.2})O_2$:10F NTs as compared to 2D thin film of $(Sn_{0.8}Ir_{0.2})O_2$:10F and thin film of pure IrO_2 electrocatalysts [1]. In addition, $(Sn_{0.8}Ir_{0.2})O_2$:10F NTs exhibit lower R_e (~0.8 Ω cm^2) as compared to thin films of $(Sn_{0.8}Ir_{0.2})O_2$:10F and thin film of pure IrO_2
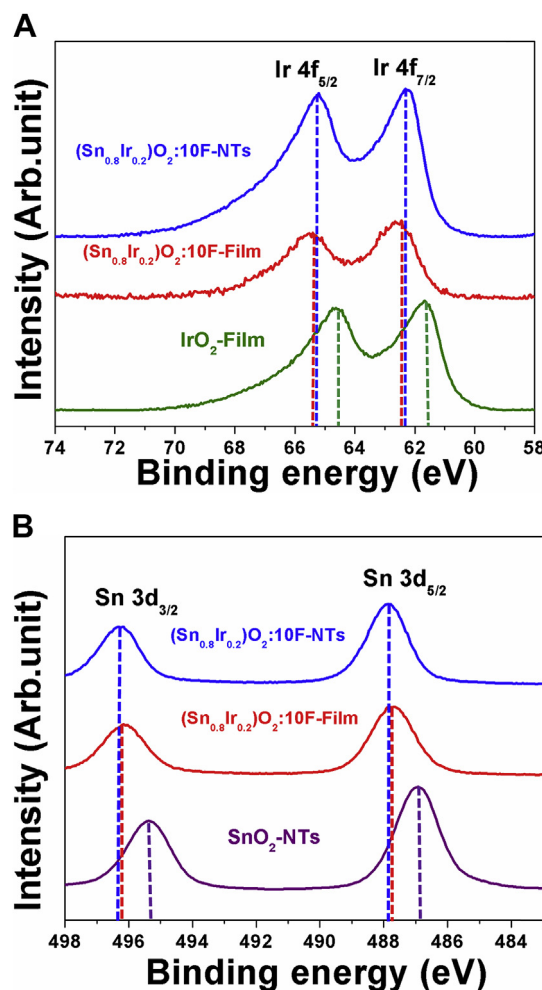
Fig. 4. The XPS spectra of (A) Ir $4f_{7/2}$ and $4f_{5/2}$ doublet and (B) Sn $3d_{5/2}$ and Sn $5d_{3/2}$ doublet of as-synthesized electrocatalyst.
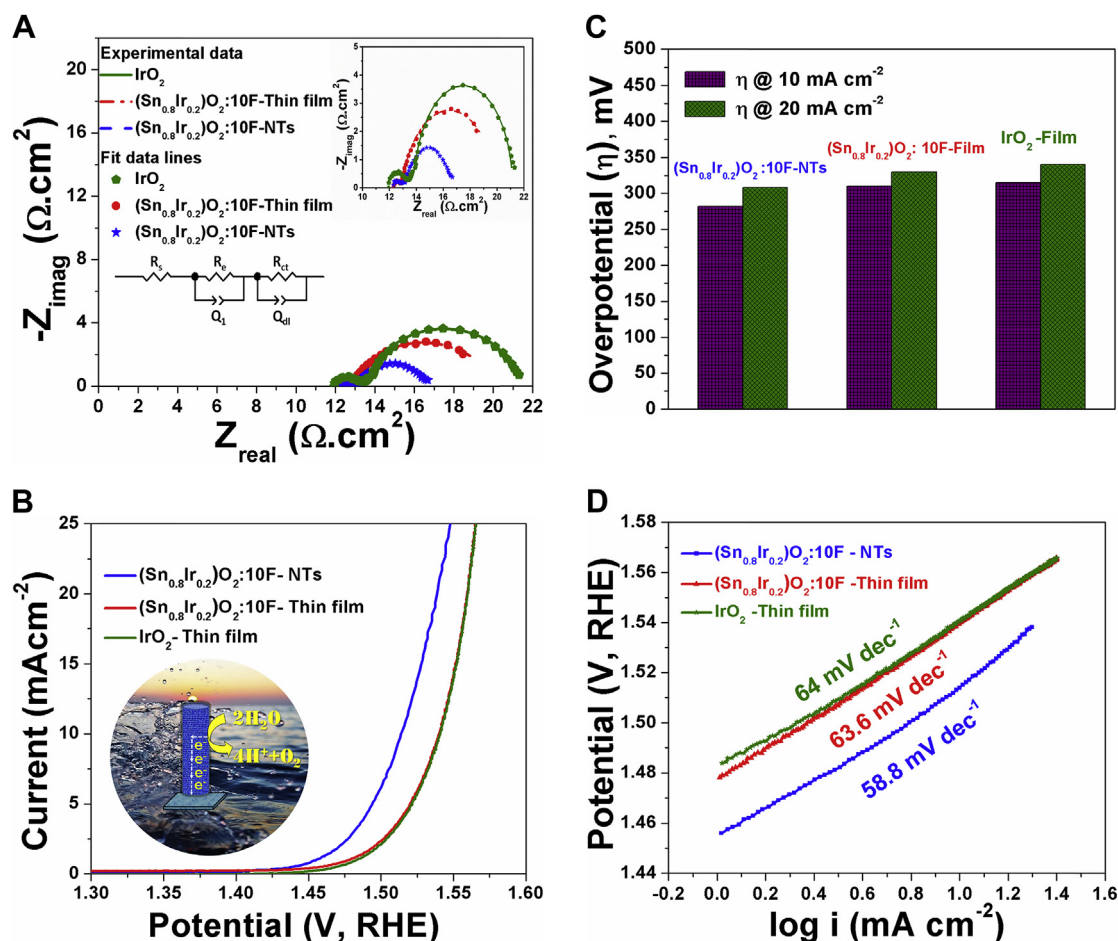
Fig. 5. (A) EIS plot of thin film of pure IrO_2, $(Sn_{0.8}Ir_{0.2})O_2$:10F and $(Sn_{0.8}Ir_{0.2})O_2$:10F NTs electrocatalysts, performed at ~1.5 V (*vs* RHE) (inset: EIS equivalent circuit and magnified view of EIS), (B) The polarization curves of $(Sn_{0.8}Ir_{0.2})O_2$:10F NTs and thin film of $(Sn_{0.8}Ir_{0.2})O_2$:10F and pure IrO_2 thin film performed in 1 N H_2SO_4 solution at 40 °C, (C) Overpotential (η in mV) required to achieve current density of 10 and 20 mAcm^{-2} and (D) Tafel plots for as-synthesized electrocatalyst.

Table 1
Results of electrochemical characterization for OER of nanostructured thin films of IrO_2 and $(Sn_{0.8}Ir_{0.2})O_2$:10F and $(Sn_{0.8}Ir_{0.2})O_2$:10F NTs, performed in 1 N H_2SO_4 electrolyte solution at 40 °C.

Electrocatalyst Composition	Onset potential V (*vs* RHE)	Current density at ~1.5 V (mA cm^{-2})	R_s ($\Omega.cm^2$)	R_e ($\Omega.cm^2$)	R_{ct} ($\Omega.cm^2$)	Tafel slope (mV dec^{-1})	Mass activity (Ag^{-1})	ECSA (m^{2}g^{-1})	TOF at ~ 1.5 V (s^{-1})
IrO_2 –Thin film	~1.43	~2.5	~12	~1.1	~8	64	8.33	29.17	0.0048
$(Sn_{0.8}Ir_{0.2})O_2$:10F –Thin film	~1.43	~2.8	~12.1	~1	~6.7	63.6	9.33	30.89	0.0068
$(Sn_{0.8}Ir_{0.2})O_2$:10F -NTs	~1.43	~6.5	~12.1	~0.8	~4.2	58.8	21.67	38.46	0.016

(Table 1). The decrease in R_{ct} and R_e for the characteristic nanotubular structure of $(Sn_{0.8}Ir_{0.2})O_2$:10F is an indicator of the improved electronic conductivity afforded by the nanotubular architecture as is known for nanotubes of other systems including Pt electrocatalysts as mentioned earlier. These results furnish the highly efficient pathway for facile charge (electron) transport on the entire $(Sn_{0.8}Ir_{0.2})O_2$:10F nanotubular electrode as well as between the electro-catalyst surface and the current collector (Ti substrate) due to the 1D vertical channels in $(Sn_{0.8}Ir_{0.2})O_2$:10F tendered by the nanotubular architecture [10,11,16]. Therefore, these experimental results collectively suggest that due to reduction in the material's dimension (i.e. from 2D to 1D), $(Sn_{0.8}Ir_{0.2})O_2$:10F NTs expedite the OER kinetics contributing to enhanced electrochemical activity as compared to the 2D thin films of $(Sn_{0.8}Ir_{0.2})O_2$:10F and pure IrO_2 [1,10,16,34].

Further electrochemical characterization has been carried out by performing the linear scan polarization of as-prepared electrodes in the electrolyte solution of 1 N H_2SO_4 at 40 °C, employing a scan rate of 10 mVs^{-1}. Fig. 5B shows the linear scan polarization curves of as-prepared electrocatalyst for OER. The onset potential of OER for $(Sn_{0.8}Ir_{0.2})$ O_2:10F NTs is ~1.43V (*vs* RHE, w.r.t. the equilibrium OER potential, 1.23V *vs* RHE) which is consistent with the nanostructured thin films of $(Sn_{0.8}Ir_{0.2})O_2$:10F and pure IrO_2 [1](Fig. 5B and Table 1). The current density obtained at ~1.5V *vs* RHE (typical potential considered to evaluate electrocatalytic performance of the electrocatalysts) for $(Sn_{0.8}Ir_{0.2})O_2$:10F NTs is ~6.5 mA cm^{-2}, which is ~2.3 and ~2.6 fold higher than that of thin films of $(Sn_{0.8}Ir_{0.2})O_2$:10F (~2.8 mA cm^{-2}) and pure IrO_2 (~2.5 mA cm^{-2}), respectively (Fig. 5B and Table 1). However, as expected, pure SnO_2 NTs exhibited extremely poor OER electrocatalytic activity (~50 μAcm^{-2} at ~1.5V *vs* RHE) (Fig. S1a, Supplementary Information). This insignificant OER activity is indeed attributed to the considerably higher charge transfer resistance of SnO_2 NTs (R_{ct} > 2000 Ω cm^2) (Fig. S1b), which indicates its poor electronic

conductivity (i.e. semiconductor nature) [47].

Furthermore, it can be seen in Fig. 5C that $(Sn_{0.8}Ir_{0.2})O_2$:10F NTs approach the current density of $10\,mA\,cm^{-2}$ and $20\,mA\,cm^{-2}$ with a lesser overpotential (η) of ~285 and 308 mV, respectively (w.r.t. the equilibrium OER potential, 1.23 V *vs* RHE). On the other hand, thin films of $(Sn_{0.8}Ir_{0.2})O_2$:10F and IrO_2 require a relatively higher overpotential of ~310 mV and 315 mV, respectively to deliver the current density of $10\,mA\,cm^{-2}$ (Fig. 5C). Further, as shown in Table 1 (see the Supplementary Information for calculation details) $(Sn_{0.8}Ir_{0.2})O_2$:10F NTs exhibited a mass activity of $21.67\,A\,g^{-1}$, specific activity of ~$0.005633\,mA\,cm^{-2}$ and TOF of $0.016\,s^{-1}$ at ~1.5V *vs* RHE (i.e. η = 0.27 V). It is noteworthy that the OER mass activity, specific activity as well as TOF value of $(Sn_{0.8}Ir_{0.2})O_2$:10F NTs is about 2–2.6 fold higher than that of thin films motifs of $(Sn_{0.8}Ir_{0.2})O_2$:10F and pure IrO_2 at the potential of ~1.5V *vs* RHE. Thus, these results clearly indicate the intrinsically higher electrocatalytic activity of $(Sn_{0.8}Ir_{0.2})O_2$:10F NTs towards water oxidation reaction (OER) as compared to the $(Sn_{0.8}Ir_{0.2})O_2$:10F and IrO_2 thin films electrocatalysts. This superior

electro-catalytic activity of $(Sn_{0.8}Ir_{0.2})O_2$:10F NTs can be ascribed to the enhancement in the OER kinetics [34] i.e. lower R_{ct} (i.e. facile charge transport along the 1D vertical channels of NTs) than the as-prepared thin film based electrocatalysts. Further, the lower Tafel slope of $(Sn_{0.8}Ir_{0.2})O_2$:10F NTs ($58.8\,mV\,dec^{-1}$) (Fig. 5D and Table 1) as compared to the thin films of $(Sn_{0.8}Ir_{0.2})O_2$:10F ($63.6\,mV\,dec^{-1}$) and IrO_2 ($64\,mV\,dec^{-1}$), suggests favorable OER kinetics i.e. likely faster electron transport and enhanced electrical conductivity/electrocatalytic activity owing to the nanotubular structure; translating to the superior OER kinetics for $(Sn_{0.8}Ir_{0.2})O_2$:10F NTs as compared to the as-synthesized thin film electrocatalyst architectures. The Tafel slope obtained for thin films of $(Sn_{0.8}Ir_{0.2})O_2$:10F and IrO_2 are relatively similar to each other, indicating similar OER kinetics.

Furthermore, to shed light on the superior electrocatalytic activity of $(Sn_{0.8}Ir_{0.2})O_2$:10F NTs and compare it with the thin films of $(Sn_{0.8}Ir_{0.2})O_2$:10F and state-of-the art IrO_2, the electrochemically active surface area (ECSA) was evaluated. The ECSA was measured from the double-layer capacitance (C_{dl}) and the linear slope of the current
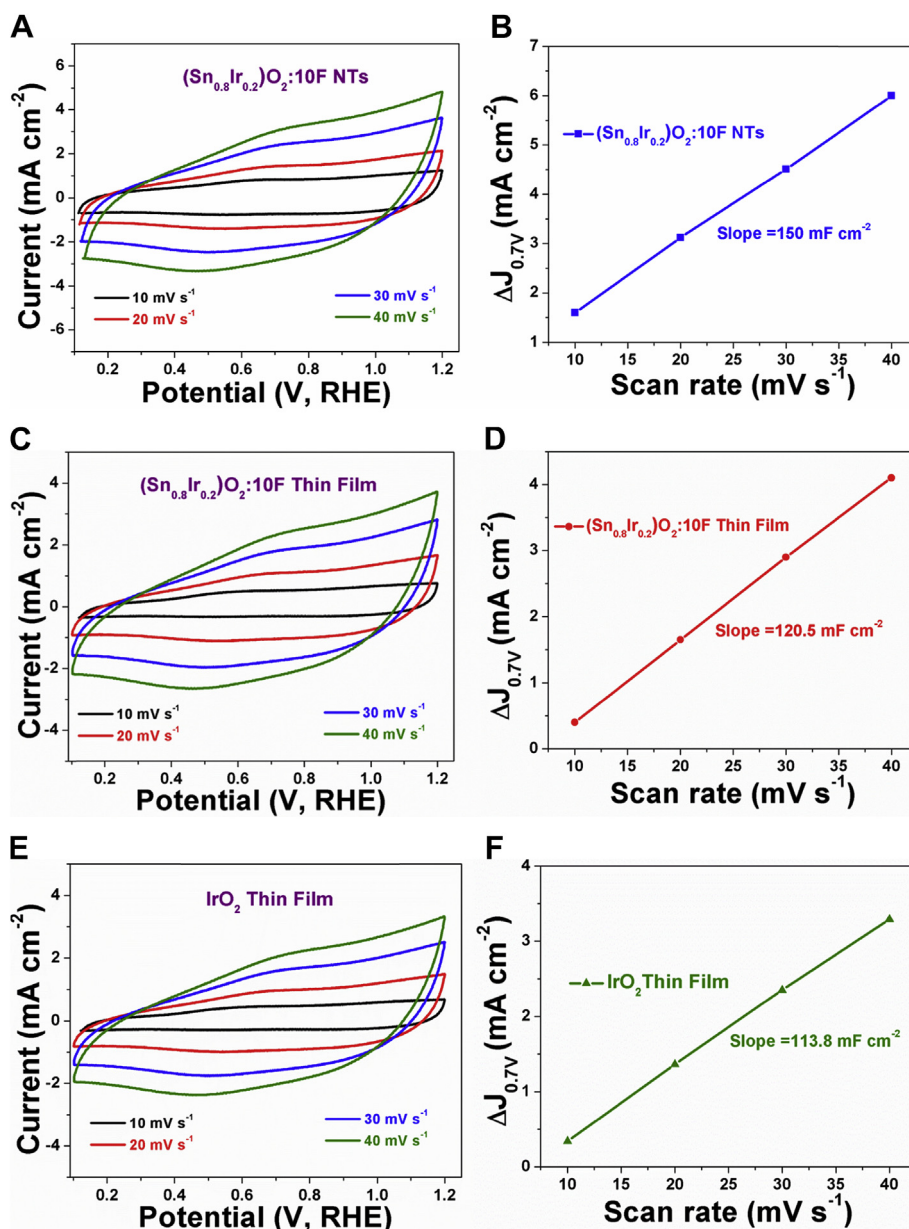

Fig. 6. CV curves and differences in current density ($j_{anode} - j_{cathode}$) at 0.7 V (*vs* RHE) plotted against scan rate and fitted to a linear regression for (A–B) $(Sn_{0.8}Ir_{0.2})O_2$:10F NTs, (C–D) $(Sn_{0.8}Ir_{0.2})O_2$:10F Thin film, and (E–F) IrO_2 thin film.

density ($j_{anode} - j_{cathode}$) *vs* scan rate (which is equivalent to twice the double layer capacitance, C_{dl}) was used to characterize the ECSA (Fig. 6 A–F), following previous reports in the literature [37,38,48–50]. It is noteworthy to mention that the obtained slope for $(Sn_{0.8}Ir_{0.2})O_2$:10F NTs ($\sim 150\,mF\,cm^{-2}$) (Fig. 6B) is considerably higher than the $(Sn_{0.8}Ir_{0.2})O_2$:10F thin film ($120.5\,mF\,cm^{-2}$) (Fig. 6D) and IrO_2 thin film ($113.8\,mF\,cm^{-2}$) (Fig. 6F), which clearly suggests the higher C_{dl}, and thereby higher ECSA for $(Sn_{0.8}Ir_{0.2})O_2$:10F NTs and comparable ECSA (electrocatalytic activity) for thin films of $(Sn_{0.8}Ir_{0.2})O_2$:10F and IrO_2. This higher ECSA presumably results from the relatively higher surface-to-volume ratio of the highly ordered nanotubes and thus, suggesting an another reflection of the superior electrochemical performance compared to the as-prepared thin film based electrocatalysts [9,38,48,49,51]. The ECSA (m^2g^{-1}) of the $(Sn_{0.8}Ir_{0.2})O_2$:10F NTs was calculated as $\sim 38.46\,m^2g^{-1}$, higher than that of $(Sn_{0.8}Ir_{0.2})O_2$:10F thin film ($\sim 30.89\,m^2g^{-1}$) and IrO_2 thin film ($\sim 29.17\,m^2g^{-1}$), respectively (details are shown in the supplementary information), which further accentuates and confirms the superior presence of effective active sites [17] on the $(Sn_{0.8}Ir_{0.2})O_2$:10F NTs.

Herein, the calculated ECSA values (m^2g^{-1}) are not very high in comparison to the surface area obtained by BET for F doped SnO_2 (173 m^2g^{-1}) [52] and Ir substituted nanopowder (100–200 m^2g^{-1}) [36,40,53,54] based oxide materials reported in the literature. In this regard, recent study conducted by Jung et al. [55], sheds light on such discrepancy in the area values (m^2g^{-1}) obtained by the ECSA and BET gas adsorption for the crystalline metal oxide OER catalysts having similar crystal structure. According to this study, to investigate the intrinsic/specific activities of the electrocatalysts, a recommended practice is to report both ECSA and BET surface area values and normalization of activity data by the areas obtained by BET and ECSA. However, it should be noted that, as electrocatalysts synthesized in the present study are directly grown/fabricated on the current collector (Ti) with the thin film structure, it is not feasible to measure the BET surface area (m^2g^{-1}) and accurately compare it with ECSA value (m^2g^{-1}) of the as-prepared electrocatalyst materials. Therefore, to gain precise insights into the intrinsic OER activity of as-prepared electrocatalysts, the current densities have been normalized by utilizing the calculated ECSA (m^2g^{-1}) and mass loading of the electrocatalysts ($0.3\,mgcm^{-2}$), and the respective OER performance was evaluated (see the Supplementary Information for calculation details). It can be seen that, the ECSA normalized current density (Fig. 7A) and mass activity (Fig. 7B) for $(Sn_{0.8}Ir_{0.2})O_2$:10F NTs is significantly higher than the $(Sn_{0.8}Ir_{0.2})$ O_2:10F and IrO_2 thin films, which reflects the higher intrinsic OER activity of NTs, which can be attributed to the higher accessible surface area as well as the intrinsic activity of each accessible site [40,52]. It should be also noted that in the present study (as described in the supplementary information), the specific capacitance (C^*) of single crystal IrO_2 (100) $\sim 650\,\mu F/cm^2$ [50,56] is used to evaluate ECSA of pure IrO_2 thin film as well as ECSA of $(Sn_{0.8}Ir_{0.2})O_2$:10F NTs and $(Sn_{0.8}Ir_{0.2})O_2$:10F thin film, which is on the basis of the isoelectronic characteristic of pure IrO_2 and $(Sn_{0.8}Ir_{0.2})O_2$:10F [1]. Thus, it should be noted that it is possible that if the actual specific capacitance (C^*) of single crystal/monolayer are determined and selected for $(Sn_{0.8}Ir_{0.2})$ O_2:10F NTs and $(Sn_{0.8}Ir_{0.2})O_2$:10F thin film, the actual ECSA values will be more representative (details are shown in the supplementary information). Therefore, as evidenced from the higher-electrochemical active surface area, specific activity, TOF and lower charge transfer resistance and Tafel slope, $(Sn_{0.8}Ir_{0.2})O_2$:10F NTs exhibit superior electrocatalytic activity towards OER as compared to the film architectures of the $(Sn_{0.8}Ir_{0.2})O_2$:10F and IrO_2 electro-catalysts.

3.1.2.1. Electrochemical stability/durability test. Long term electrochemical stability is an imperative criterion for the high performance OER electrocatalysts in terms of their commercial applications. Herein, the electrochemical stability of $(Sn_{0.8}Ir_{0.2})O_2$:10F NTs, $(Sn_{0.8}Ir_{0.2})O_2$:10F thin film and IrO_2 thin film electrocatalysts was

studied by performing the chronoamperometry (CA) test for OER at the constant potential of $\sim 1.5\,V$ (*vs* RHE) in 1 N H_2SO_4 at 40 °C for 24 h. As shown in Fig. 8, $(Sn_{0.8}Ir_{0.2})O_2$:10F NTs exhibit higher current owing to the exceptional electrochemical activity discussed above. However, more importantly what is clearly apparent is the excellent long term electrochemical stability, similar to $(Sn_{0.8}Ir_{0.2})O_2$:10F thin film as well as pure IrO_2 thin film with a minimal loss in current density [1]. It is noteworthy to mention that the F doped $(Sn,Ir)O_2$ solid solution electrocatalyst with different morphologies (NTs and thin film) and similar composition [$(Sn_{0.8}Ir_{0.2})O_2$:10F] exhibits comparable electrochemical stability under identical operating conditions. This can be attributed to the unique electronic structure obtained upon F containing solid solution formation of $(Sn,Ir)O_2$:F [1,57]. As reported earlier by us [5], more negative cohesive energy (E_{coh}) is obtained upon solid solution formation due to the stronger bond dissociation energy for Sn-O bonds ($-528\,kJ\,mol^{-1}$) than Ir-O bonds ($-414\,kJ\,mol^{-1}$) [58]. Further, the E_{coh} of the F doped $(Sn,Ir)O_2$ solid solution electrocatalyst becomes equal to that of pure IrO_2 approximately at ~ 8–10 wt% of F as shown earlier [5]. Thus, these previous theoretical studies have demonstrated that introduction of F modifies the overall electronic structure of the system in such a manner that the electrochemical performance of the doped surface becomes similar to the surface of the pure IrO_2, suggesting the beneficial role of F in the as-synthesized electrocatalysts. This is indeed observed experimentally and the observed stability (Fig. 8) wherein $(Sn_{0.8}Ir_{0.2})O_2$:10F exhibits excellent electrochemical stability in both nanotubular and thin film morphologies, identical to that of pure IrO_2.

In addition, the approach of using F as a doping agent to enhance the stability of the oxide electrocatalysts is seen to be positive as
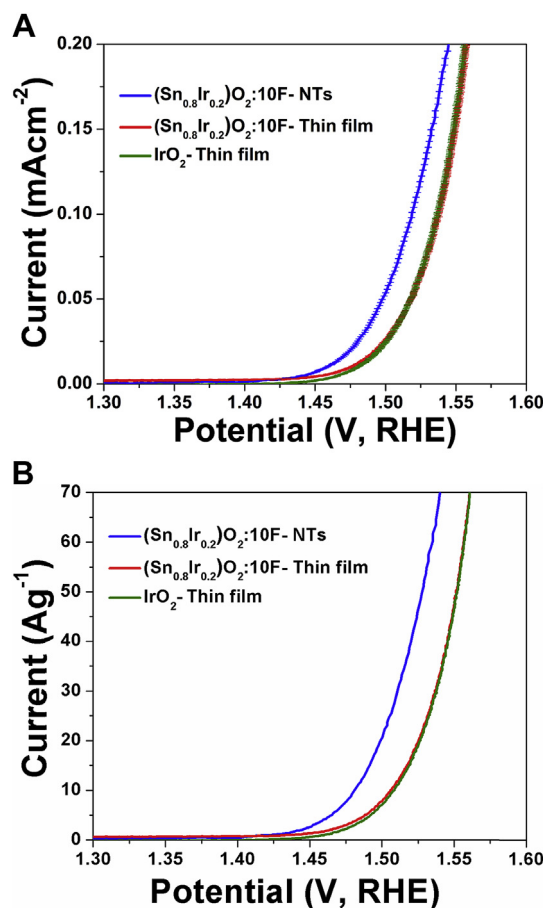
Fig. 7. The Current density curves of $(Sn_{0.8}Ir_{0.2})O_2$:10F NTs and thin film of $(Sn_{0.8}Ir_{0.2})O_2$:10F and IrO_2, normalized by (A) respective ECSA ($m^2\,g^{-1}$) and (B) electrocatalyst mass loading.
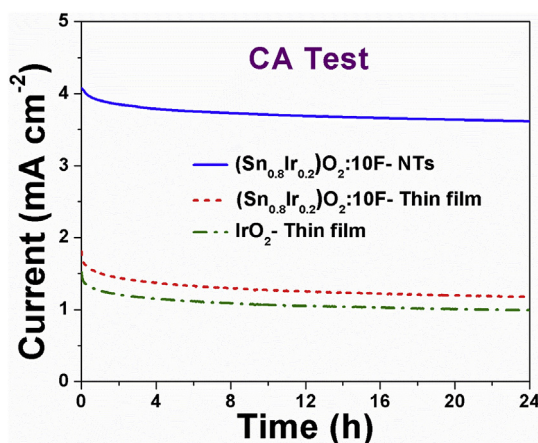
Fig. 8. The chronoamperometry (CA) test of $(Sn_{0.8}Ir_{0.2})O_2$:10F NTs and thin films of $(Sn_{0.8}Ir_{0.2})O_2$:10F and pure IrO_2 electrocatalysts conducted in 1 N H_2SO_4 solution under a constant potential of $\sim$ 1.5 V (*vs* RHE) at 40 °C for 24 h.

reportedly confirmed by various studies [57,59,60]. The stabilizing effect of F on the transition metal oxide based supports such as tin (Sn) has also been thoroughly investigated by various groups. For example, Geiger et al. [57] conducted the investigation of the potential dependent dissolution rates of various catalyst supports such as fluorine doped tin oxide (FTO), indium tin oxide (ITO) and antimony doped tin oxide (ATO) in the broad potential window ranging from -0.6 to 3.2 V RHE in 0.1 M H_2SO_4 electrolyte. Their study concludes that FTO exhibits best electrochemical stability with no sign for any measurable catalysts dissolution in the potential limits of -0.34 V RHE < E < 2.7 V RHE, making FTO as an appropriate candidate for electro-catalyst supports for acidic OER. Besides, in the theoretical study by Binninger et al. [61], it has been reported that oxygen anion-free salts containing anion species with a very high oxidation potential such as fluorides, chlorides, or sulfates are promising candidates for thermodynamically stable OER. Thus, our obtained results are indeed in good agreement with these reported studies, wherein the incorporation of F in the high Sn: Ir ratio (80:20) containing solid solution electrocatalysts exhibit superior activity as well as excellent electrochemical stability for acidic OER.

Furthermore, inductively coupled plasma - optical emission spectroscopy (ICP-OES) analysis conducted on the 1 N H_2SO_4 electrolyte solution after the 24 h CA test shows very low ($\sim$ 0 ppm) dissolution of Ir and Sn for the as-prepared $(Sn_{0.8}Ir_{0.2})O_2$:10F NTs and thin films of $(Sn_{0.8}Ir_{0.2})O_2$:10F and IrO_2 electro-catalysts (see Table S2 for ICP-OES results) [1]. Therefore, in addition to the superior electrocatalytic activity of $(Sn_{0.8}Ir_{0.2})O_2$:10F NTs, the ICP-OES results suggest the excellent robustness of $(Sn_{0.8}Ir_{0.2})O_2$:10F NTs towards OER in PEM water electrolysis. Further, to investigate the possible structural changes occurring during the OER durability test, XRD and XPS analysis for the $(Sn_{0.8}Ir_{0.2})O_2$:10F NTs was carried out after performing the 24 h OER chronoamperometry test. As shown in Fig. S2 (Supplementary Information), the XRD pattern of the $(Sn_{0.8}Ir_{0.2})O_2$:10F NTs did not feature any major change in the rutile type tetragonal structure, suggesting structural properties are considerably unaffected during the OER process [62]. Further, in the XPS spectra recorded after 24 h chronoamperometry test (Figs. S3a–b, Supplementary Information), the stable $(Sn_{0.8}Ir_{0.2})O_2$:10F NTs contained Ir and Sn. The Sn 3d signal of $(Sn_{0.8}Ir_{0.2})O_2$:10F NTs post stability exhibited appearance of Sn $3d_{3/2}$ and Sn $3d_{5/2}$ with similar binding energies values as those in the as-synthesized fresh electrode (Fig. S3a). However, in the case of XPS spectra of Ir (Fig. S3b) corresponding to $(Sn_{0.8}Ir_{0.2})O_2$:10F NTs following post stability tests, it is interesting to note that Ir $4f_{5/2}$ and Ir $4f_{7/2}$ doublet positions exhibited slight negative shift of $\sim$ 0.25 eV (i.e. towards lower binding energy) as compared to the corresponding doublet

positions of the as-synthesized fresh $(Sn_{0.8}Ir_{0.2})O_2$:10F NTs. This negative shift in the XPS suggests the formation of sub-stoichiometric IrO_2 i.e. partial conversion of IrO_2 to hydrated sub-stoichiometric IrO_x species [62,63]. Similar behavior in the XPS analysis for the Ir signal was observed in the recent study by Siracusano et al. [62]. Such negative shift in binding energy values can be attributed to beneficial surface modification occurring during the high rate of oxygen evolution reaction. In addition, the role of hydrated structures arising from such surface modification is well known to stimulate the OER kinetics [60,62,64,65]. Thus, the as-performed post stability characterization results suggest the excellent robustness and beneficial surface modification of $(Sn_{0.8}Ir_{0.2})O_2$:10F NTs towards prolonged OER in the PEM based water splitting process.

Consequently, the above electrochemical results demonstrate that the rational fabrication of earth abundant SnO_2, F and ultra-low noble metal (Ir) containing solid solution electrocatalyst with the nanotubular functionalities indeed enhances the electrocatalytic activity and offers a unique opportunity to tailor the electronic, physical and electrocatalytic properties of $(Sn,Ir)O_2$:10F. Strikingly, it turns out that our $(Sn_{0.8}Ir_{0.2})O_2$:10F electrocatalyst - directly grown on the current collector represents a novel highly active electrode configuration for OER. This is owing to the facile pathway for electron transport aided by the likely improved electronic conductivity i.e. low surface charge transfer resistance (R_{ct}) and presence of 1D vertical channels contributing the high electrochemical active surface area (ECSA) and thus, attainment of excellent electrochemical performance towards OER in PEM water electrolysis.

4. Conclusions

In summary, the present study demonstrates the suitability of 1D vertically aligned nanotubes (VANTs) of $(Sn_{0.8}Ir_{0.2})O_2$:10F as a potential electrocatalyst system for oxygen evolution reaction (OER) in PEM based water electrolysis. The VANTs of $(Sn_{0.8}Ir_{0.2})O_2$:10F fabricated on Ti substrate exhibit excellent electrochemical performance with significant $\sim$ 2.3 and $\sim$ 2.6 times higher electrocatalytic activity than that of the 2D thin film architectures of identical composition of $(Sn_{0.8}Ir_{0.2})O_2$:10F and state-of-the-art IrO_2 electrocatalysts, respectively. In addition, $(Sn_{0.8}Ir_{0.2})O_2$:10F NTs displayed lower surface charge transfer resistance ($\sim$4.2 Ω cm^2), lower Tafel slope (58.8 mV dec^{-1}), higher electrochemical active surface area (38.46 m^2 g^{-1}), higher mass (21.67 A g^{-1}) and specific activity (0.005633 mA cm^{-2}) and higher TOF (0.016 s^{-1}) than the as-synthesized benchmark IrO_2 and $(Sn_{0.8}Ir_{0.2})O_2$:10F thin film based electrocatalysts. Moreover, the as-prepared $(Sn_{0.8}Ir_{0.2})O_2$:10F NTs demonstrate excellent electrochemical stability in the harsh acidic media - identical to that of IrO_2 and $(Sn_{0.8}Ir_{0.2})O_2$:10F thin film electrocatalyst, operated for OER under similar conditions. Thus, the present study contributes the major enhancement in the electrocatalytic performance of $(Sn_{0.8}Ir_{0.2})O_2$:10F composition contrasted with nanostructured 2D thin film by fabricating 1D vertically aligned nanotubular architectures with substantial reduction in Ir content ($\sim$ 80 mol.%). The superior performance will ultimately likely result in reduction in overall capital cost of water splitting process. Therefore, the as-prepared $(Sn_{0.8}Ir_{0.2})O_2$:10F NTs reported herein are indeed promising as an OER electrocatalyst for generation of highly efficient and sustainable hydrogen via PEM based water electrolysis.

Conflicts of interest

There are no conflicts of interest to declare.

Appendix A. Supplementary data

Supplementary data related to this article can be found at http://dx.doi.org/10.1016/j.jpowsour.2018.04.065.

References

[1] M.K. Datta, K. Kadakia, O.I. Velikokhatnyi, P.H. Jampani, S.J. Chung, J.A. Poston, A. Manivannan, P.N. Kumta, J. Mater. Chem. 1 (2013) 4026–4037.
[2] P.P. Patel, P.J. Hanumantha, O.I. Velikokhatnyi, M.K. Datta, B. Gattu, J.A. Poston, A. Manivannan, P.N. Kumta, Mater. Sci. Eng., B 208 (2016) 1–14.
[3] S.A. Grigoriev, V.I. Porembsky, V.N. Fateev, Int. J. Hydrogen Energy 31 (2006) 171–175.
[4] S.D. Ghadge, P.P. Patel, M.K. Datta, O.I. Velikokhatnyi, R. Kuruba, P.M. Shanthi, P.N. Kumta, RSC Adv. 7 (2017) 17311–17324.
[5] K. Kadakia, M.K. Datta, O.I. Velikokhatnyi, P.H. Jampani, P.N. Kumta, Int. J. Hydrogen Energy 39 (2014) 664–674.
[6] K. Kadakia, M.K. Datta, O.I. Velikokhatnyi, P. Jampani, S.K. Park, S.J. Chung, P.N. Kumta, J. Power Sources 245 (2014) 362–370.
[7] L. Trotochaud, J.K. Ranney, K.N. Williams, S.W. Boettcher, J. Am. Chem. Soc. 134 (2012) 17253–17261.
[8] Y. Lu, S. Du, R. Steinberger-Wilckens, Appl. Catal. B Environ. 199 (2016) 292–314.
[9] P. Chen, K. Xu, Z. Fang, Y. Tong, J. Wu, X. Lu, X. Peng, H. Ding, C. Wu, Y. Xie, Angew. Chem. 127 (2015) 14923–14927.
[10] G. Liu, J. Xu, Y. Wang, X. Wang, J. Mater. Chem. 3 (2015) 20791–20800.
[11] C.-L. Zhang, S.-H. Yu, Chem. Soc. Rev. 43 (2014) 4423–4448.
[12] S.M. Bergin, Y.-H. Chen, A.R. Rathmell, P. Charbonneau, Z.-Y. Li, B.J. Wiley, Nanoscale 4 (2012) 1996–2004.
[13] K. Gong, F. Du, Z. Xia, M. Durstock, L. Dai, Science 323 (2009) 760.
[14] C. Koenigsmann, S.S. Wong, Energy Environ. Sci. 4 (2011) 1161–1176.
[15] Q.-Z. Jiang, X. Wu, M. Shen, Z.-F. Ma, X.-Y. Zhu, Catal. Lett. 124 (2008) 434–438.
[16] Y. Kim, J.G. Kim, Y. Noh, W.B. Kim, Catal. Surv. Asia 19 (2015) 88–121.
[17] G. Zhang, S. Sun, M. Cai, Y. Zhang, R. Li, X. Sun, Sci. Rep. 3 (2013).
[18] P.P. Patel, P.J. Hanumantha, O.I. Velikokhatnyi, M.K. Datta, D. Hong, B. Gattu, J.A. Poston, A. Manivannan, P.N. Kumta, J. Power Sources 299 (2015) 11–24.
[19] C. Zhao, H. Yu, Y. Li, X. Li, L. Ding, L. Fan, J. Electroanal. Chem. 688 (2013) 269–274.
[20] Y.G. Guo, J.S. Hu, H.M. Zhang, H.P. Liang, L.J. Wan, C.L. Bai, Adv. Mater. 17 (2005) 746–750.
[21] H.-M. Zhang, Y.-G. Guo, L.-J. Wan, C.-L. Bai, Chem. Commun. (2003) 3022–3023.
[22] B. Xiang, P. Wang, X. Zhang, S.A. Dayeh, D.P.R. Aplin, C. Soci, D. Yu, D. Wang, Nano Lett. 7 (2007) 323–328.
[23] V.F. Puntes, K.M. Krishnan, A.P. Alivisatos, Science 291 (2001) 2115–2117.
[24] Y. Wu, P. Yang, J. Am. Chem. Soc. 123 (2001) 3165–3166.
[25] S.Y. Li, P. Lin, C.Y. Lee, T.Y. Tseng, J. Appl. Phys. 95 (2004) 3711–3716.
[26] H. Wang, L. Gao, Current Opinion in Electrochemistry 7 (2018) 7–14.
[27] F. Aziz, A.A. Bakar, Z. Ahmad, T.M. Bawazeer, N. Alsenany, M.S. Alsoufi, A. Supangat, Mater. Lett. 211 (2018) 195–198.
[28] J.R. Ota, S.K. Srivastava, Nanotechnology 16 (2005) 2415.
[29] X. Zhang, Y. Liu, Z. Kang, ACS Appl. Mater. Interfaces 6 (2014) 4480–4489.
[30] J. Chung, J. Myoung, J. Oh, S. Lim, J. Phys. Chem. C 114 (2010) 21360–21365.
[31] L.E. Greene, B.D. Yuhas, M. Law, D. Zitoun, P. Yang, Inorg. Chem. 45 (2006) 7535–7543.
[32] P.R. Zafred, J.T. Dederer, J.E. Gillett, R.A. Basel, A.B. Antenucci, in, Google Patents, 1996.
[33] J.A.V. Butler, Proc. Roy. Soc. Lond. Math. Phys. Sci. 157 (1936) 423–433.
[34] P.P. Patel, M.K. Datta, O.I. Velikokhatnyi, R. Kuruba, K. Damodaran, P. Jampani, B. Gattu, P.M. Shanthi, S.S. Damle, P.N. Kumta, Sci. Rep. 6 (2016).
[35] K.S. Kadakia, P. Jampani, O.I. Velikokhatnyi, M.K. Datta, S.J. Chung, J.A. Poston, A. Manivannan, P.N. Kumta, J. Electrochem. Soc. 161 (2014) F868–F875.
[36] K.S. Kadakia, P.H. Jampani, O.I. Velikokhatnyi, M.K. Datta, S.K. Park, D.H. Hong, S.J. Chung, P.N. Kumta, J. Power Sources 269 (2014) 855–865.
[37] H. Liang, F. Meng, M. Cabán-Acevedo, L. Li, A. Forticaux, L. Xiu, Z. Wang, S. Jin, Nano Lett. 15 (2015) 1421–1427.
[38] Y. Tong, J. Xu, J. Jiang, F. Gao, Q. Lu, Chem. Eng. J. 316 (2017) 225–231.
[39] K. Kadakia, M.K. Datta, O.I. Velikokhatnyi, P. Jampani, S.K. Park, P. Saha, J.A. Poston, A. Manivannan, P.N. Kumta, Int. J. Hydrogen Energy 37 (2012) 3001–3013.
[40] M. Bernicke, E. Ortel, T. Reier, A. Bergmann, J. Ferreira de Araujo, P. Strasser, R. Kraehnert, ChemSusChem 8 (2015) 1908–1915.
[41] S. Geiger, O. Kasian, B.R. Shrestha, A.M. Mingers, K.J.J. Mayrhofer, S. Cherevko, J. Electrochem. Soc. 163 (2016) F3132–F3138.
[42] D.F. Abbott, D. Lebedev, K. Waltar, M. Povia, M. Nachtegaal, E. Fabbri, C. Copéret, T.J. Schmidt, Chem. Mater. 28 (2016) 6591–6604.
[43] K. Kadakia, M.K. Datta, P.H. Jampani, S.K. Park, P.N. Kumta, J. Power Sources 222 (2013) 313–317.
[44] P.P. Patel, P.J. Hanumantha, O.I. Velikokhatnyi, M.K. Datta, B. Gattu, J.A. Poston, A. Manivannan, P.N. Kumta, Mater. Sci. Eng., B 208 (2016) 1–14.
[45] W.K. Choi, H.J. Jung, S.K. Koh, J. Vac. Sci. Technol.: Vacuum, Surfaces, and Films 14 (1996) 359–366.
[46] O.I. Velikokhatnyi, K. Kadakia, M.K. Datta, P.N. Kumta, J. Phys. Chem. C 117 (2013) 20542–20547.
[47] R. Kötz, S. Stucki, B. Carcer, J. Appl. Electrochem. 21 (1991) 14–20.
[48] X. Sun, L. Gao, C. Guo, Y. Zhang, X. Kuang, T. Yan, L. Ji, Q. Wei, Electrochim. Acta 247 (2017) 843–850.
[49] J. Yu, F.-X. Ma, Y. Du, P.-P. Wang, C.-Y. Xu, L. Zhen, ChemElectroChem 4 (2017) 594–600.
[50] T. Hepel, F.H. Pollak, W.E. O'Grady, J. Electrochem. Soc. 132 (1985) 2385–2390.
[51] H. Wang, C. Xu, F. Cheng, M. Zhang, S. Wang, S.P. Jiang, Electrochem. Commun. 10 (2008) 1575–1578.
[52] H.S. Oh, H.N. Nong, P. Strasser, Adv. Funct. Mater. 25 (2015) 1074–1081.
[53] H.N. Nong, H.S. Oh, T. Reier, E. Willinger, M.G. Willinger, V. Petkov, D. Teschner, P. Strasser, Angew. Chem. Int. Ed. 54 (2015) 2975–2979.
[54] H.-S. Oh, H.N. Nong, T. Reier, M. Gliech, P. Strasser, Chem. Sci. 6 (2015) 3321–3328.
[55] S. Jung, C.C.L. McCrory, I.M. Ferrer, J.C. Peters, T.F. Jaramillo, J. Mater. Chem. 4 (2016) 3068–3076.
[56] B.M. Tackett, W. Sheng, S. Kattel, S. Yao, B. Yan, K.A. Kuttiyiel, Q. Wu, J.G. Chen, (2018).
[57] S. Geiger, O. Kasian, A.M. Mingers, K.J.J. Mayrhofer, S. Cherevko, Sci. Rep. 7 (2017) 4595.
[58] Y.-R. Luo, Comprehensive Handbook of Chemical Bond Energies, CRC press, 2007.
[59] T. Binninger, R. Mohamed, K. Waltar, E. Fabbri, P. Levecque, R. Kötz, T.J. Schmidt, Sci. Rep. 5 (2015).
[60] T. Reier, Z. Pawolek, S. Cherevko, M. Bruns, T. Jones, D. Teschner, S.r. Selve, A. Bergmann, H.N. Nong, R. Schlögl, J. Am. Chem. Soc. 137 (2015) 13031–13040.
[61] T. Binninger, R. Mohamed, K. Waltar, E. Fabbri, P. Levecque, R. Kötz, T.J. Schmidt, Sci. Rep. 5 (2015) 12167.
[62] S. Siracusano, V. Baglio, S.A. Grigoriev, L. Merlo, V.N. Fateev, A.S. Aricò, J. Power Sources 366 (2017) 105–114.
[63] J.F. Moulder, W.F. Stickle, P.E. Sobol, K.D. Bomben, Eden Prairie, MN, (1995) 119.
[64] V. Pfeifer, T.E. Jones, J.J.V. Vélez, C. Massué, M.T. Greiner, R. Arrigo, D. Teschner, F. Girgsdies, M. Scherzer, J. Allan, Phys. Chem. Chem. Phys. 18 (2016) 2292–2296.
[65] S. Cherevko, S. Geiger, O. Kasian, N. Kulyk, J.-P. Grote, A. Savan, B.R. Shrestha, S. Merzlikin, B. Breitbach, A. Ludwig, Catal. Today 262 (2016) 170–180.